

MASTER OT J072007.30+451611.6: A Polar with Strong Optical Variability and Suppressed He II Emission

A. V. Bobakov,^{1*} S. V. Zharikov,² A. V. Karpova,¹ D. A. Zyuzin,¹ A. Yu. Kirichenko,^{2,1} Yu. A. Shibano,¹ R. Karimov,³ N. L. Vaidman,^{4,5} Sh. T. Nurmakhmetova,⁴ M. R. Gilfanov,^{6,7} and R. Michel²

¹*Ioffe Institute, 26 Politekhnicheskaya, St. Petersburg, 194021, Russia*

²*Instituto de Astronomía, Universidad Nacional Autónoma de México, Apdo. Postal 106, Baja California, México, 22860*

³*Ulugh Beg Astronomical Institute, Uzbekistan Academy of Sciences, Tashkent, 100052, Uzbekistan*

⁴*Faculty of Physics and Technology, Al-Farabi Kazakh National University, Al-Farabi Ave., 71, 050040, Almaty, Kazakhstan*

⁵*Fesenkov Astrophysical Institute, Observatory, 23, Almaty, 050020, Kazakhstan*

⁶*Space Research Institute of the Russian Academy of Sciences, Profsoyuznaya Str. 84/32, 117997 Moscow, Russia*

⁷*Max-Planck-Institut für Astrophysik, Karl-Schwarzschild-Str. 1, D-85741 Garching, Germany*

Accepted XXX. Received YYY; in original form ZZZ

ABSTRACT

The transient optical source MASTER OT J072007.30+451611.6 has been recently discovered and proposed as a peculiar polar with an unusually high amplitude of the orbital brightness variation in the optical of ~ 3 mag. To clarify its nature, we performed multiband time-series optical photometry with 1.5-m class telescopes and spectroscopy with the 10.4-m Gran Telescopio Canarias. We also analysed archival data of different optical surveys and detected the source in X-rays with the Spectrum-RG/*eROSITA* telescope. We confirm the orbital period of ≈ 1.5 h with the high amplitude of the brightness modulation. Compiling survey data, covering ~ 19 yr, we find high and low brightness states of the object at time scales of years, likely explained by different accretion rates. Our data were obtained in the high brightness state. Optical spectra with hydrogen and helium emission lines, consisting of broad and narrow components, indicate the presence of an accretion stream without disk. The Doppler tomography shows that the narrow component is mainly emitted from the Lagrangian L_1 point, while the broad component is from the region where the accretion stream interacts with the white dwarf magnetosphere. The ratio of equivalent widths of He II 4686 and H β emission lines is < 0.4 , which is curiously low for polars. The X-ray spectrum of the source can be described by the thermal plasma emission model with parameters consistent with values observed for polars.

Key words: binaries: close – novae, cataclysmic variables – stars: individual: MASTER OT J072007.30+451611

1 INTRODUCTION

MASTER OT J072007.30+451611.6 (hereafter J0720) is an unusual non-eclipsing compact binary system recently discovered by Pogrosheva et al. (2018); Denisenko (2018). The optical data from the Catalina Sky Survey (CSS; Drake et al. 2009) showed a large-amplitude (~ 3 mag) variability with the periodicity of 0.0627887 d (1.50693 h; Denisenko 2018). The J0720 low-resolution optical spectrum was obtained in the Large Sky Area Multi-Object Fiber Spectroscopic Telescope (LAMOST, Zhao et al. 2012) survey¹. It demonstrates relatively narrow Balmer emission lines which can be a marker of an accretion process in the system. In addition, the source has an X-ray counterpart² designated as XMMSL2 J072007.4+451615 in the *XMM-Newton* Slew Survey Clean Source Catalog (XMMSLEW-CLN; Saxton et al. 2008). Its observed flux in the 0.2–12 keV range is $(2.9 \pm 1.0) \times 10^{-12}$ erg s^{−1} cm^{−2}.

Denisenko (2018) classified J0720 as a polar or AM Herculis-type cataclysmic variable (CV). Polars represent a subclass of magnetic CVs (mCVs) in which the accreting white dwarf (WD) has a high magnetic field, ~ 10 – 100 MG, which prevents the formation of an accretion disc (e.g. Cropper 1990). In this case, the accretion matter streams from the donor star directly along the magnetic field lines of the WD to its magnetic pole(s). We note that such strong optical orbital variability of J0720 is not typical for polars. Usually, they show orbital variations of $\lesssim 2$ mag. In addition, polars may switch between high and low accretion states, which strongly alters their brightness. Denisenko (2018) suggested that the highly modulated optical light curve of J0720 results from a large contribution of a hot spot at the WD surface.

There is another class of highly variable binaries with similar orbital periods, which consist of non-accreting millisecond pulsars and low-mass companions dubbed ‘spider pulsars’ (e.g. Draghis et al. 2019; Mata Sánchez et al. 2023; Bobakov et al. 2024). Their optical variability, typically of ≈ 2 – 4 mag, is a result of the strong irradiation of the secondary by the pulsar wind. Optical spectra of some ‘spiders’ demonstrate H and He emission lines, which can be attributed to the stellar wind and/or intrabinary shock (e.g. Swihart et al. 2022).

* E-mail: bobakovalex@gmail.com

¹ <https://www.lamost.org/dr8/v2.0/spectrum/view?obsid=504804160>

² <https://www.aavso.org/vsx/index.php?view=detail.top&oid=621224>

Table 1. Log of the J0720 photometric observations.

Date	MJD	Filter	Exp. time
MAO			
2023-11-12	60260	<i>V</i>	120 s × 17
		<i>V</i>	180 s × 57
		<i>R</i>	180 s × 22
		<i>I</i>	180 s × 22
OAN-SPM			
2023-11-26	60274	<i>V</i>	600 s × 11
			300 s × 5
			400 s × 1
		<i>R</i>	200 s × 6
			300 s × 11
		<i>I</i>	200 s × 1
			150 s × 2
			90 s × 16
2023-12-12	60290	<i>V</i>	300 s × 1
		<i>R</i>	60 s × 17
			100 s × 3
2023-12-13	60291	<i>V</i>	300 s × 27
		<i>R</i>	100 s × 28
		<i>I</i>	60 s × 28
2023-12-14	60292	<i>V</i>	300 s × 19
		<i>R</i>	100 s × 19
		<i>I</i>	60 s × 19
ATO			
2025-01-10	60685	<i>r</i>	20 s × 964
2025-01-13	60688	<i>i</i>	20 s × 402

Note. MAO and OAN-SPM observations were performed with Johnson-Cousins filters and ATO – with Sloan ones.

To investigate the nature of J0720, we have performed its optical time-resolved photometric and spectroscopic observations. We also considered optical data from different catalogues and X-ray data from the *eROSITA* telescope (Predehl et al. 2021) onboard the Spectrum–RG (SRG) observatory (Sunyaev et al. 2021). The catalogue data and our own observations are described in Sec. 2 and analysed in Sec. 3. We discuss and summarise the results in Sec. 4.

2 OBSERVATIONS AND DATA REDUCTION

2.1 Catalogue data

We found that J0720 is present in different optical catalogues. As noted in Denisenko (2018), it was identified as CSS J072007.4+451615 in the CSS catalogue. In addition, in the *Gaia* DR 3 catalogue (Gaia Collaboration et al. 2016, 2023) J0720 is designated as 974157681483861248, and has the coordinates R.A. = 07^h20^m07^s.3812(5), Dec. = +45°16′11″507(1) and the mean magnitude $G = 20.9$. No parallax measurements were reported for the source. It is also identified in the Panoramic Survey Telescope and Rapid Response System (Pan-STARRS) DR 2 catalogue (Flewelling et al. 2020), the AllWISE Source Catalog (WISEA, Wright et al. 2019) and the Zwicky Transient Facility (ZTF, Masci et al. 2019) DR 22 archive data. The Pan-STARRS and ZTF data confirm the strong variability of J0720 previously identified in the CSS data (Fig. 1).

Table 2. Log of the J0720 spectroscopic observations with the GTC.

Date	MJD	Grism	Range, Å	Exp. time
2024-02-03	60343.1001	R1000B	3630–7000	400 s × 4
2024-11-03	60617.1329	R2000B	3950–5700	535 s × 10
	60617.1986	R2500R	5575–7685	530 s × 10

2.2 Optical photometry and spectroscopy

The time-series photometry of J0720 was performed using 1.5-m telescopes at the Maidanak Astronomical Observatory (MAO) in Uzbekistan, Assy-Turgen observatory (ATO) in Kazakhstan, and Observatorio Astronómico Nacional San Pedro Mártir (OAN-SPM) in Mexico. Standard data reduction and photometric calibrations were applied using a set of Pan-STARRS field stars around the target and corresponding IRAF tasks. The log of observations is given in Table 1.

The time-series spectroscopy was performed with the 10.4-m Gran Telescopio Canarias (GTC). The first run of long-slit observations was carried out in February 2024 through the Director’s Discretionary Time (DDT)³ with the upgraded Optical System for Imaging and low-intermediate Resolution Integrated Spectroscopy (OSIRIS+) instrument. We obtained four consecutive spectra with an exposure time of 400 s using the R1000B grism through the 0.8 arcsec slit. The resulting spectral resolution was 5.4 Å. We obtained an additional set of observations in November 2024⁴ using the same instrument and the R2000B and R2500R grisms. The full binary orbit was covered with ten consecutive exposures for each grism. The spectral resolutions were 4.4 Å (R2000B) and 3.4 Å (R2500R). The log of observations is given in Table 2.

The data reduction was performed with the semi-automated pipeline packages PYEIT (Prochaska et al. 2020a; Prochaska et al. 2020b) and IRAF. Flux calibration was achieved using the Feige 110 spectrophotometric standard.

2.3 X-ray data

The J0720 field was observed by the SRG/*eROSITA* in the course of four all-sky surveys in 2020–2021 with the total vignetting corrected exposure time of ≈ 440 s. *eROSITA* data were calibrated and processed by the calibration pipeline at the Space Research Institute (IKI) based on the *eROSITA* Science Analysis Software System (eSASS) (Brunner et al. 2022) and pre- and in-flight calibration data.

3 DATA ANALYSIS AND RESULTS

3.1 Long- and short-term variability in the optical

The long-term brightness variation of J0720 collected by different photometric sky surveys is shown in Fig. 1. It covers the time interval from 2005 to 2024. It can be seen that the source demonstrates high (MJD ≈ 53400 –56000 and 58200–60500) and low (MJD ≈ 56000 –57000) brightness states. In the high state, it is strongly variable with $\Delta\text{mag} \sim 3$ –4 mag, apparently at time scales from several days to months. Transitions between high and low states are typical for mCVs (e.g. Latham et al. 1981), while they are not observed for ‘spider’ systems.

We applied the Lomb-Scargle periodogram (Lomb 1976; Scargle

³ Program GTC11-23BDDT, PI A. Kirichenko.

⁴ Program GTC1-24BMEX, PI S. Zharikov.

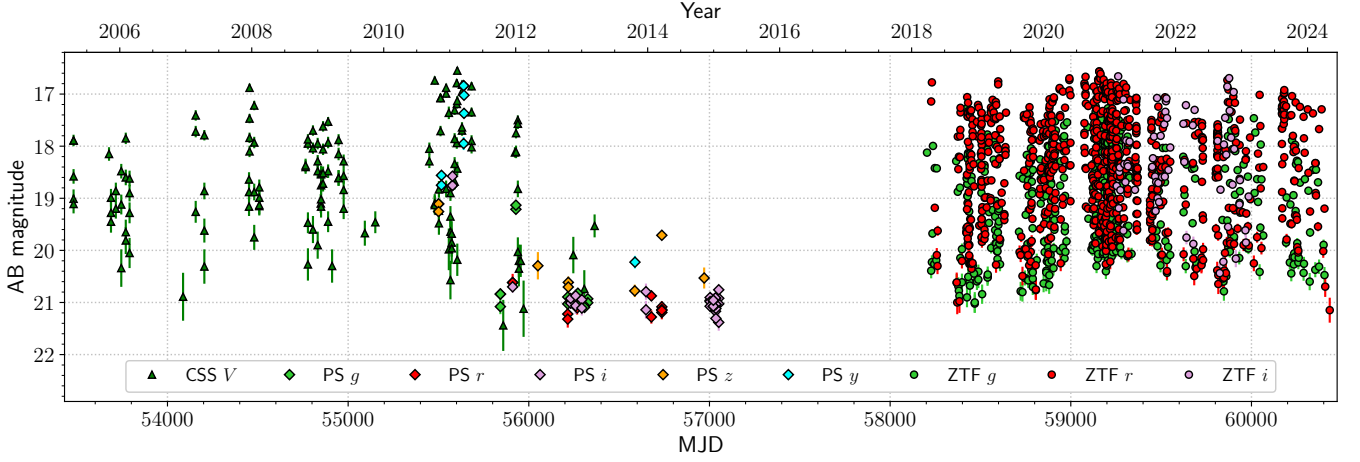


Figure 1. J0720 light curves obtained from the CSS, Pan-STARRS and ZTF data, demonstrating changes between high and low brightness states. Data from different surveys and bands are shown by various symbols as indicated in the legend (PS = Pan-STARRS).

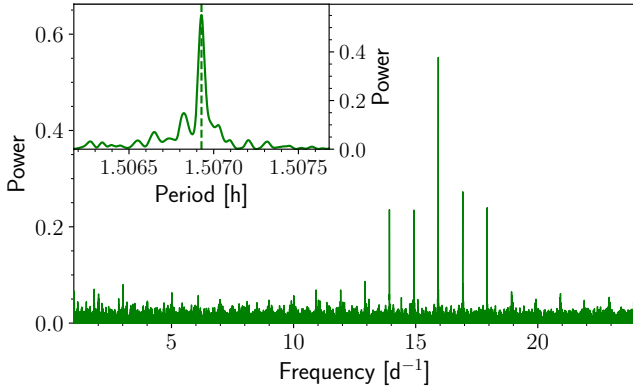


Figure 2. Lomb-Scargle periodogram calculated for the ZTF data in the r band. The best period corresponding to the highest peak, enlarged in the inset, is indicated by the dashed line.

1982) analysis to search for periodicity in the r -band ZTF data, which spans over six years and contains about 800 measurements. The resulting power spectrum is shown in Fig. 2. The highest peak $f_{\text{ph}} = 15.92644(25) \text{ d}^{-1}$ corresponds to the period⁵ $P_{\text{ph}} = 1.506928(24) \text{ h}$. It is in agreement with the value reported by Denisenko (2018) and proposed as the orbital period P_{orb} of the system. The ZTF, ATO, MAO, and OAN-SPM data folded with the obtained period are shown in Fig. 3 (the zero phase corresponds to $t_0 = \text{HJD } 2460617.620472$ which was selected from spectroscopy and Doppler tomography; see below). All the light curves are consistent in shape and demonstrate strong asymmetry with a fast increase of the brightness, a plateau state at maximum brightness with small amplitude flickering during $\approx 0.3P_{\text{orb}}$ followed by a more gradual decline in brightness until the minimum lasting $\approx 0.4P_{\text{orb}}$. There is a hint of an intermediate minimum during brightness decline. Comparison of the amplitude of orbital brightness variations with those in Fig. 1 indicates that J0720 was in the high state during our photometric observations.

⁵ The uncertainty is calculated as the half width at half maximum of the highest peak in the periodogram.

3.2 Optical spectra

In Fig. 4, we show J0720 optical spectra obtained at orbital phases near the maximum and minimum of the object’s brightness marked by vertical lines in the left-top panel of Fig. 3. The spectra demonstrate strong Balmer emission lines, which have been seen in the LAMOST data. In addition, weaker He I and He II emission lines are detected. The object shows substantial continuum variability with the highest amplitude in the 5000–7000 Å range, that decreases to the bluer and redder parts of the spectrum and disappears below 4000 Å. To check the brightness state of J0720 during the spectroscopy runs, we extracted magnitudes from the spectral data obtained in November 2024 using the Pan-STARRS g -filter transmission curve and a simple rectangular filter with the wavelength range of 5600–7400 Å partially overlapping with the r band. The results are presented in the top and middle subpanels of Fig. 3, left. The obtained light curves are compatible with the photometric ones, which shows that J0720 was in the high state during the spectral observations as well. The four spectra obtained in February 2024 are consistent with the November ones at close orbital phases.

In Fig. 5, we demonstrate the trailed spectra folded with the orbital period for each grism. The emission lines clearly show a sine-like variability of their positions, depending on radial velocities (RVs) of the emitting matter, with the orbital phase. These variations look similar for different lines. The lines have highly variable asymmetric profiles indicating the presence of at least two emission components (Fig. 6). Such profiles with two or three components are typical for polars (e.g. Schwöpe et al. 1997). Accounting for our limited spectral resolution, we tried to fit profiles in each phase bin with a combination of two Gaussian functions. To do this, we used the Markov chain Monte Carlo procedure (Foreman-Mackey et al. 2013). We found that one Gaussian is narrower and less intense (‘narrow’) than the other one (‘broad’). Some examples of the fit results are presented in Fig. 6. As seen, the components are most clearly resolved near the orbital phase ~ 0.8 . Variations of the best-fitting parameters with the orbital phase for the H α line are shown in Fig. 7. We then fitted RVs of each component by the sine function:

$$v_i(t) = \gamma_i + K_i \sin\left(\frac{2\pi(t - t_0)}{P_{\text{orb}}} - \Delta\phi_i\right), \quad i \in \{\text{narrow, broad}\}, \quad (1)$$

where t is time, γ_i is the systemic RV, K_i is the RV semi-amplitude,

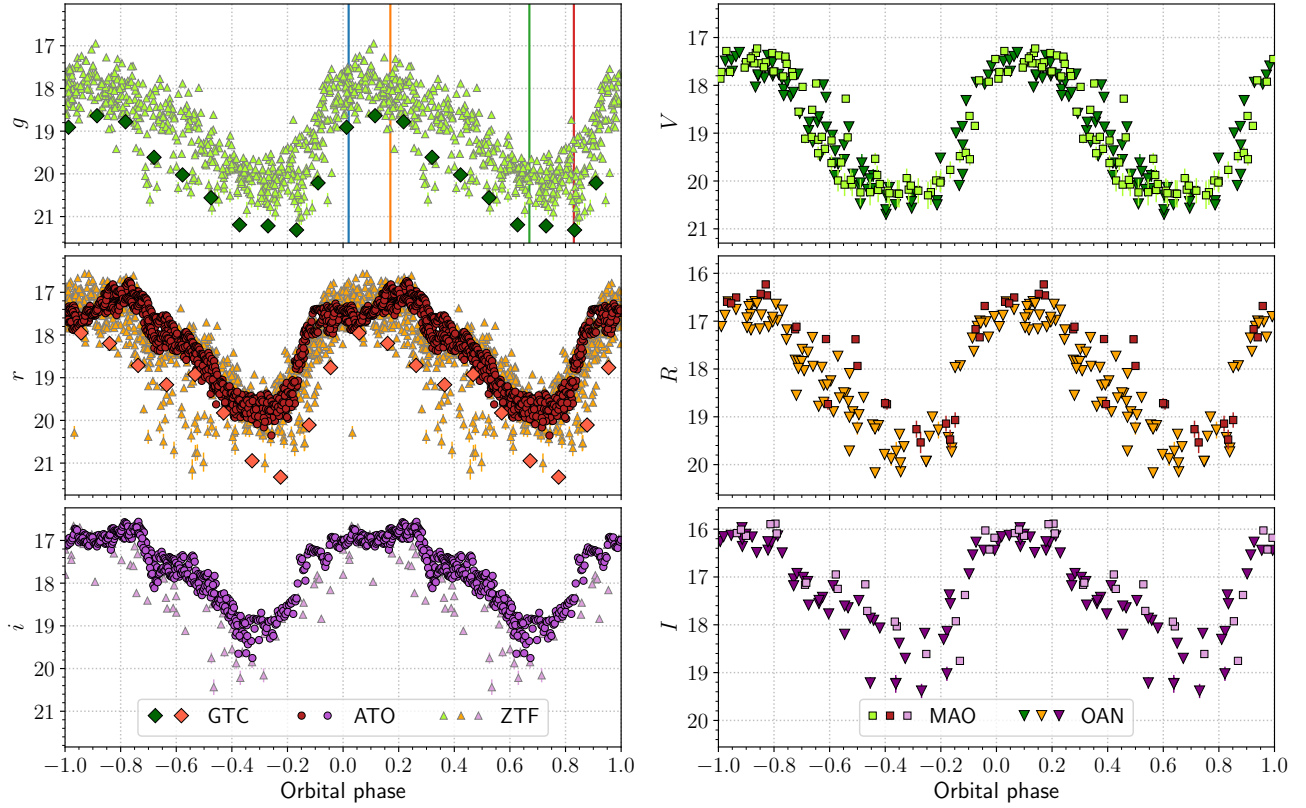


Figure 3. Light curves of J0720 folded with the period of 1.506928 h. Data from different instruments are marked with different symbols as indicated in the legends. ZTF and ATO measurements, as well as magnitudes obtained from the GTC spectra in the AB system, are presented in the left panels, while MAO and OAN-SPM measurements in the Vega system – in the right panels. Two periods are shown for clarity. The zero phase was selected based on spectroscopic data (see text below). Vertical colour lines in the top left panel mark the phases at which the spectra shown in Fig. 4 were obtained.

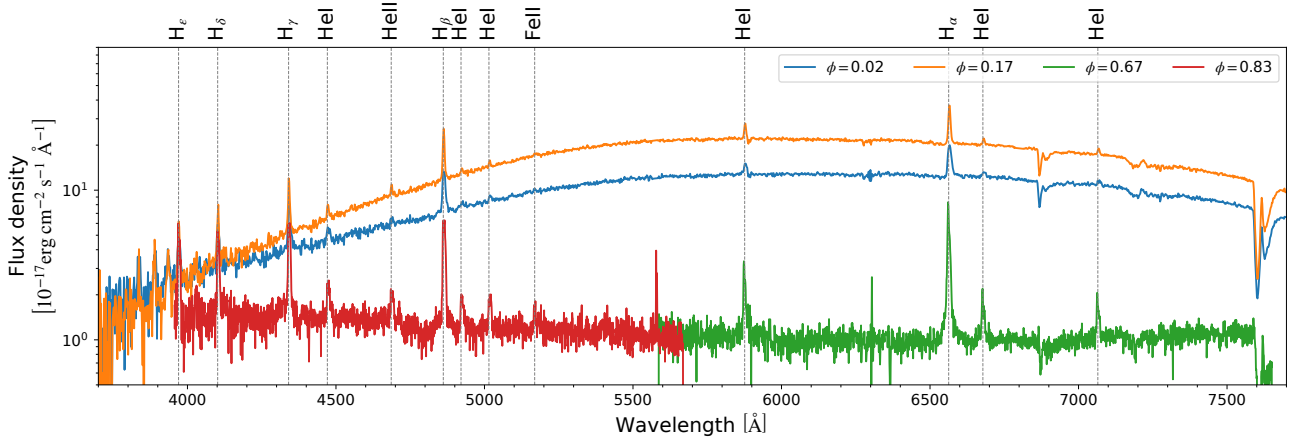


Figure 4. Optical spectra of J0720 obtained at different orbital phases with the GTC using R1000B (orange and blue), R2000B (red) and R2500R (green) grisms.

$\Delta\phi_i$ is the phase shift relative to the time t_0 . The results for $H\alpha$ and $H\beta$ lines are presented in Fig. 7, Fig. 8 and Table 3.

Both components of Balmer lines demonstrate RVs curves with practically similar amplitudes but shifted from one to another in orbital phase by about 0.25. Their peak intensities and FWHMs only marginally vary with the orbital phase at $\sim 1\sigma$ level. A high degeneracy between these parameters thus precludes any reliable analysis of their orbital variations. At the same time, maxima of full

Balmer line intensities are reached at the phase of the maximum of the object photometric brightness ($\phi \approx 0.1$; Fig. 8).

He lines are much weaker than the Balmer ones, and therefore, their fit results are too uncertain.

In polars, narrow Balmer, He I, and He II lines likely arise from the tip of the Roche lobe of the donor star and possibly the beginning of the accretion stream, while the broad ones trace the accretion regions near WD magnetic poles (Schwope et al. 2011). In addition,

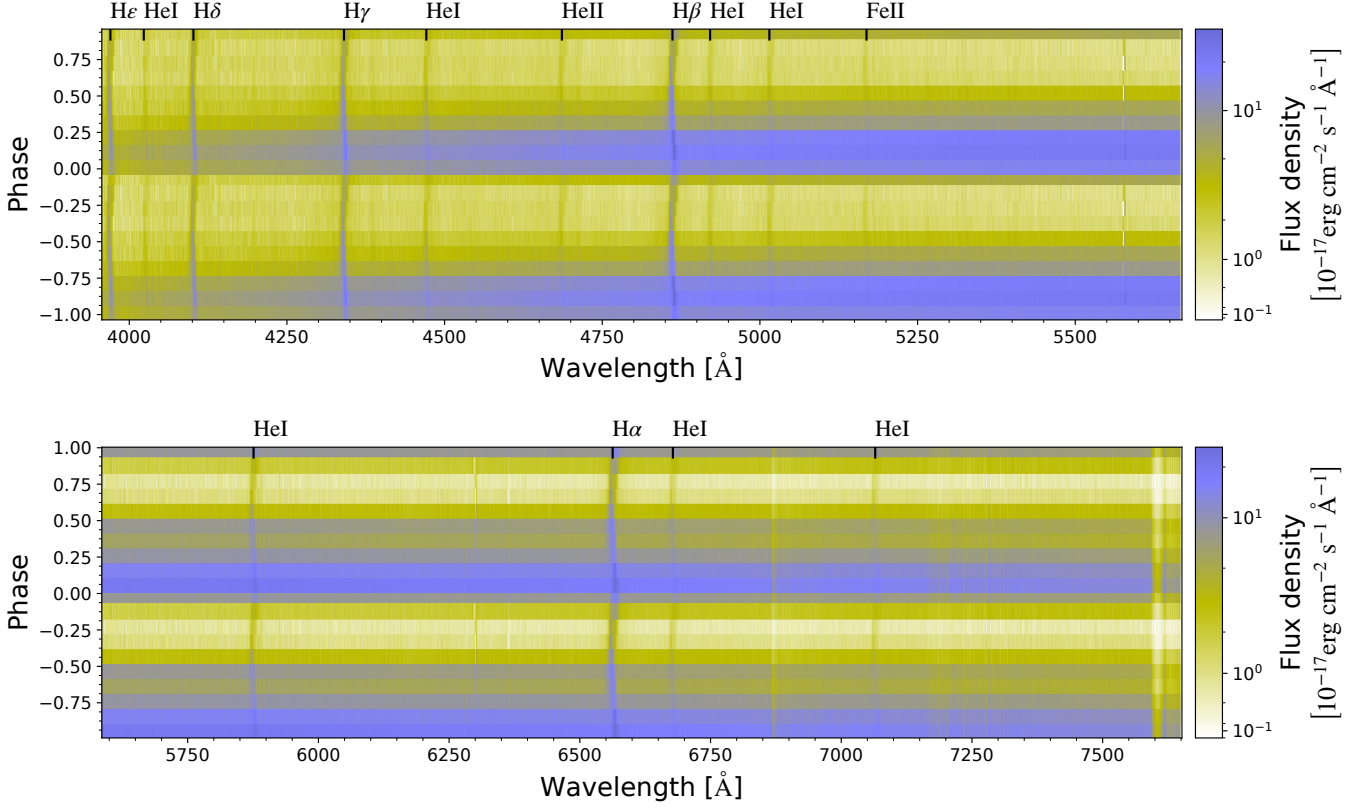


Figure 5. Trailed spectra of J0720 obtained with R2000B (top) and R2500R (bottom) grisms. Two orbital cycles are presented for clarity.

Table 3. Best-fitting parameters with 1σ uncertainties for the RV curves of spectral line components.

Line	Component	γ , km s $^{-1}$	K , km s $^{-1}$	$\Delta\phi$
H α	broad	141 ± 25	221 ± 36	0.25 ± 0.02
	narrow	100 ± 32	190 ± 41	0.01 ± 0.02
H β	broad	140^{+31}_{-30}	184^{+43}_{-42}	0.26 ± 0.04
	narrow	100 ± 25	173^{+112}_{-98}	0.04 ± 0.05

the donor is irradiated by the WD. This is typically observed via Na I 8183, 8195 doublet and Ca II 8498 and 8542 emission lines above the accretion continuum. They are formed closer to the donor centre of mass, however, they are located outside our observed range. Artistic representations of the system at three specific orbital phases are shown at the top of Fig. 7. At phase 0.0 the WD magnetic polar region hot spot is located on the line of sight of the observer.

3.3 System parameters

The light curves and spectral properties allow us to state that J0720 is likely a polar. To estimate the system parameters, we thus accepted the WD mass $M_1 = 0.8 M_\odot$ which is the average value for mCVs (Shaw et al. 2020). From the mass-period and the radius-mass relationships

given by Smith & Dhillon (1998)

$$\frac{M_2}{M_\odot} = (0.126 \pm 0.011)P_{\text{orb}} - (0.110 \pm 0.040), \quad (2)$$

$$\frac{R_2}{R_\odot} = (0.117 \pm 0.004)P_{\text{orb}} - (0.011 \pm 0.018), \quad (3)$$

where P_{orb} represents the orbital period in hours, we estimated the secondary star's mass $M_2 = 0.09 \pm 0.05 M_\odot$ and its radius $R_2 = 0.17 \pm 0.02 R_\odot$. This gives the mass ratio $M_2/M_1 \approx 0.1$. J0720 shows high optical variability, but no WD eclipses are seen in the light curves. Assuming that the H α narrow component is formed near the tip of the Roche lobe (L_1 point), given its RV semi-amplitude (Table 3) and the masses of the components we estimate the system inclination to be $i = 48^\circ \pm 12^\circ$. As we have mentioned above, the heating of the secondary star by high-energy radiation emitted from the accreting magnetic white dwarf results in formation of emission lines closer to the donor centre of mass (Davey & Smith 1992). Assuming that the narrow component velocity corresponds to the centre-of-mass velocity, we obtain the lower limit to the system inclination of about 36° .

Based on the system inclination and duration of the plateau state at maximum brightness $\Delta\phi \approx 0.3P_{\text{orb}}$, we estimated the co-latitude of the accretion spot at WD surface as

$$\beta = \arctan\left(-\frac{\cos(\pi\Delta\phi)}{\tan(i)}\right) = 28^\circ \pm 10^\circ. \quad (4)$$

It is in agreement with what is observed in single-pole accreting polars, where the co-latitude β of the accretion spot typically lies in the range 20–50 degrees (Cropper 1988).

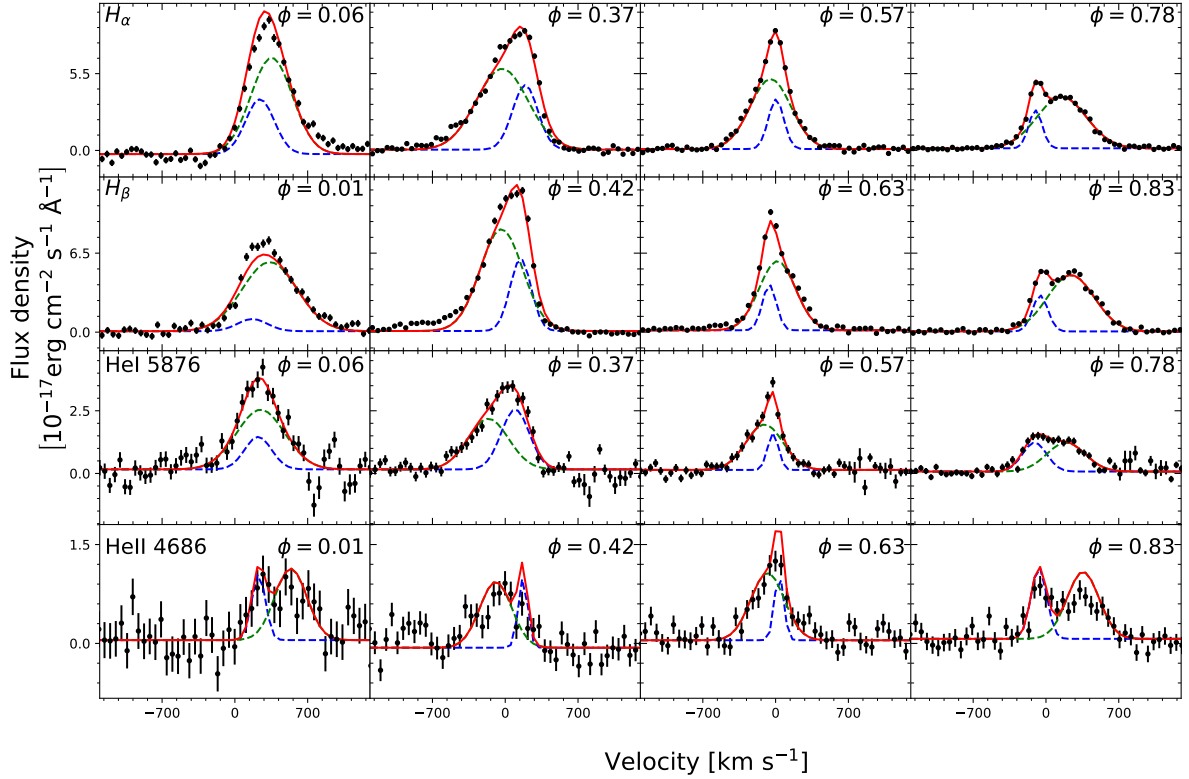


Figure 6. Profiles of two Balmer lines (two upper rows) and He (two lower rows) spectral lines at different orbital phases ϕ indicated in the panels. The black points with error bars show continuum-subtracted data. In each panel, the red solid line is the best-fitting double-Gaussian model. The blue and green dashed lines show the best fit components of the model.

3.4 Doppler tomography

We used the Doppler tomography technique (Marsh & Horne 1988) to probe the accretion flow structure in J0720. This technique is a well-known method to map the emission of gas moving in the velocity space (V , θ), where V is the absolute value of the velocity measured relative to the system's centre of mass and θ is the angle between the velocity vector and the line between the centres of mass of the primary and secondary stars. We generated Doppler maps from the GTC time-resolved spectra using the maximum entropy method (Sruuit 1998) as implemented by Kotze et al. (2016). The Roche lobe of the secondary and the primary, the positions of centres of mass of stars and the system, and the ballistic trajectory of the accreted matter are calculated using the system parameters. The results for the $H\alpha$ line are presented in Fig. 9. In the bottom panels of the figure, the standard and inside-out projection tomograms are displayed. They reveal a relatively bright compact and a more extended emission regions. The zero phase is a free parameter and it was fixed to locate the emission maximum of the compact region at the L_1 point, i.e. at the beginning of the ballistic stream, as observed in eclipsing polars (Schwope et al. 1997; Salvi et al. 2002). This gives $t_0 = \text{HJD } 2460617.620472$. In this case, the more extended emission is distributed between the ballistic trajectory and the boundary of the WD Roche lobe, and the maximum of its intensity is shifted by $\approx 0.25P_{\text{orb}}$ in respect to the L_1 point. A similar picture is obtained for other Balmer as well as He I lines.

To understand the origin of the two emission regions, we constructed model tomograms for $H\alpha$ narrow and broad components separately based on the result of the RV fit. They are presented in the top panels of Fig. 9. As expected, the narrow line component corresponds to the compact bright region at the L_1 point ($V \approx 200 \text{ km s}^{-1}$,

$\theta \approx 90^\circ$). The broad component is extended along the Roche lobe boundary away from the stream ballistic trajectory and has a compact brightest excess at $V \approx 250 \text{ km s}^{-1}$, $\theta \approx 190^\circ$.

In contrast to Balmer and He I lines, no emission spot is seen near the L_1 point for the He II 4686 line tomogram (left and middle panels of Fig. 10). For illustrative purposes, we overlay an example of magnetic trajectories following Kotze et al. (2016). We also show the system in spatial coordinates (Fig. 10, right).

3.5 X-ray spectrum

Utilising the eSASS tasks, we extracted the J0720 spectra from the *eROSITA* data in a circular region with a 60-arcsec radius. For the background extraction, we chose an annulus region around the source with the inner and outer radii of 150 and 300 arcsec. We obtained 79 net counts and grouped the spectra to ensure at least 1 count per bin.

The spectra were fitted in the 0.3–9 keV band with the X-Ray Spectral Fitting Package (XSPEC) v.12.13.1 (Arnaud 1996). Due to the low number of counts, we used the W -statistics appropriate for Poisson data with Poisson background (Wachter et al. 1979). To account for the interstellar absorption, we applied the TBABS model with the WILM abundances (Wilms, Allen & McCray 2000). According to the 3D dust map of Green et al. (2019), the maximal reddening in the J0720 direction is low, $E(B - V) = 0.05$ mag. We converted this value to the column density N_H using the empirical relation from Fought et al. (2016). The resulting value, $N_H = 4.4 \times 10^{20} \text{ cm}^{-2}$, was fixed during the fitting procedure.

We found that the spectrum can be well described by the optically thin thermal plasma model MEKAL (Mewe et al. 1985, 1986; Liedahl et al. 1995) with the temperature $T = 7^{+25}_{-4} \text{ keV}$, the unabsorbed flux

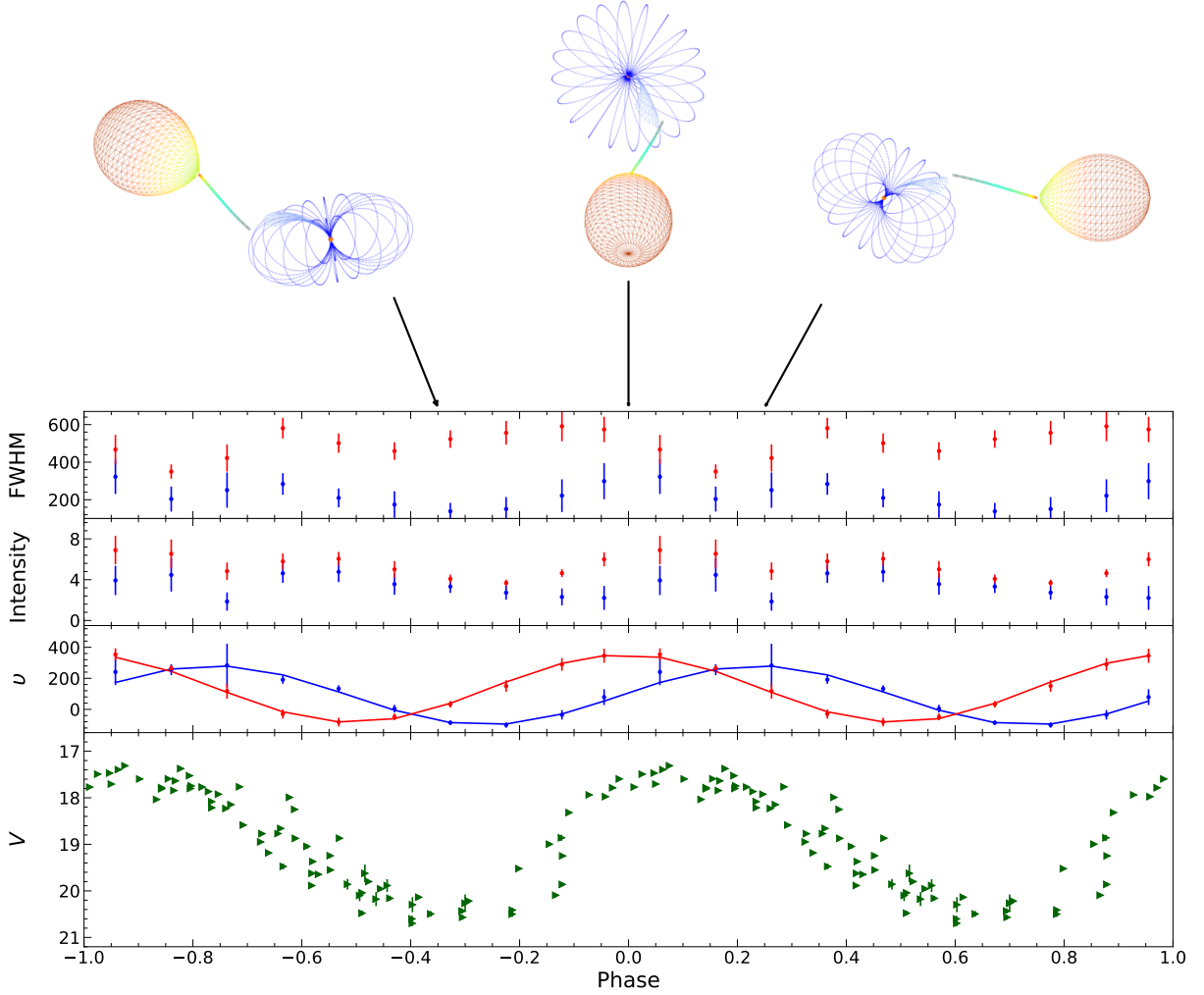


Figure 7. Variations of the best-fitting parameters for the $H\alpha$ line profiles obtained with the double Gaussian model with the orbital phase. The top panel shows FWHMs in units of km s^{-1} , the middle panel – continuum-subtracted intensities in units of $10^{-17} \text{ erg cm}^{-2} \text{ s}^{-1} \text{ \AA}^{-1}$, the third panel – RVs in units of km s^{-1} and the bottom panel – light curve in the V band. Results for the broad and narrow line components are presented in red and blue, respectively. In the third panel, lines represent the sine fits of the RV curves. At the top of the plot the artistic views on the system configuration with parameters from Sect. 3.3 in different orbital phases are shown. The size of the magnetosphere (with blue magnetic field lines), the accreting stream (green-blue), and the result of irradiation of the secondary (yellow) were selected arbitrary.

in the 0.3–10 keV band $F_X^{0.3-10 \text{ keV}} = 5.1^{+2.1}_{-1.4} \times 10^{-13} \text{ erg s}^{-1} \text{ cm}^{-2}$ and $W = 63$ for 82 degrees of freedom. The spectrum and the best-fitting model are presented in Fig. 11.

4 DISCUSSION AND CONCLUSIONS

We have analysed optical and X-ray observations of J0720. Using optical photometry and time-resolved spectroscopy, we confirmed the orbital period and high amplitude of brightness modulation of ≈ 3 mag found by Denisenko (2018). Archival optical data reveal the high and low brightness states of J0720 and it has been in the high state since at least 2018 until our observations. No evidence of eclipses or outbursts was found in the data covering the period from the end of 2023 to the beginning of 2025.

The GTC optical spectra obtained in the high state demonstrate Balmer and He I emission lines as well as unusually weak He II. The Doppler tomography revealed that J0720 is a system with an accretion stream instead of a disk which unambiguously confirms its

classification as a polar and rejects the ‘spider’ pulsar interpretation. The emission lines have asymmetric shapes and show significant profile and RV variations with the orbital phase. The line profiles can be described by a model consisting of narrow and broad components associated with different emission regions. This is a common property of polars (e.g. Beuermann et al. 2021; Liu et al. 2023; Lin et al. 2025). The RV curves of the components have similar amplitudes but are shifted by about 0.25 in phase. Such behaviour of Balmer emission lines was observed in the polar CP Tuc ($G = 19.1$ mag, $D = 207$ pc) with an orbital period of 0.061832 d, close to that of J0720 (Thomas & Reinsch 1996). The WD or donor star are not resolved in our spectra. Cyclotron humps typical for polars are not detected either, and the continuum is smooth. It varies with the orbital period, having the maximum amplitude of variation at $\sim 6000 \text{ \AA}$. This is also similar to the case of CP Tuc, though the maximal variation of its continuum is smaller (≈ 2 mag) and occurs at $\approx 8800 \text{ \AA}$.

Typically, spectra of polars show a strong He II 4686 emission line with an equivalent width (EW) comparable to that of $H\beta$ (e.g. Szkody 1998). In Fig. 12, we present variations of EWs of He II 4686 and $H\beta$

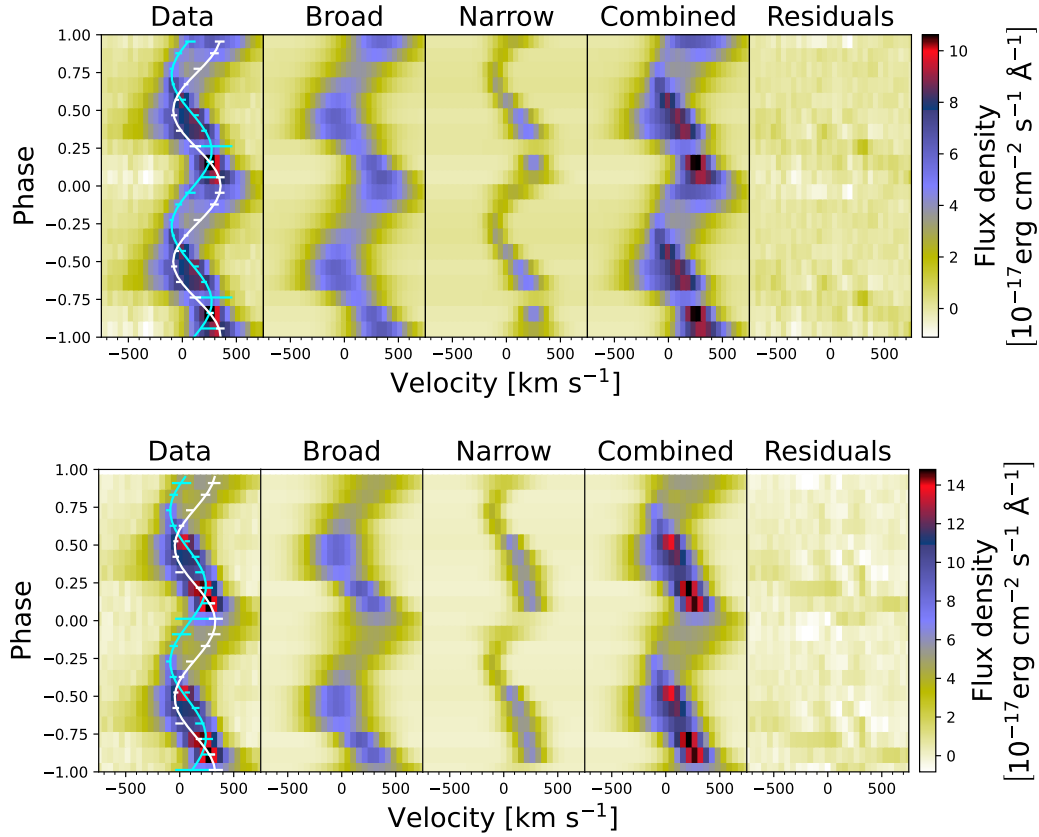


Figure 8. Trailed spectra of $H\alpha$ (top) and $H\beta$ (bottom) emission line and the results of their fitting. Two orbital cycles are presented for clarity. From left to right: data, the broad component fit, the narrow component fit, the combination of the two components, and the residuals (given as data minus model). White and cyan error bars show 1σ uncertainties of the RVs of the broad and narrow components, while solid lines represent their best-fitting sine functions.

lines⁶ as well as their ratio with the J0720 orbital phase. One can see that the EWs vary in antiphase with the source brightness while the line ratio changes roughly in phase with it. This may indicate that at the maximum brightness phase the emission comes from the hotter plasma with a higher ionisation rate from the irradiated secondary’s surface and/or the region where the stream interacts with the WD magnetosphere, forming a hot spot.

Silber (1992) provided the following criterion for separating mCVs from non-magnetic CVs: $EW(\text{He II } 4686)/EW(H\beta) > 0.4$ and $EW(H\beta) > 20 \text{ \AA}$. For J0720, the ratio $EW(\text{He II } 4686)/EW(H\beta)$ is $\lesssim 0.4$ over the whole orbital period (Fig. 12, middle) with the averaged value of ≈ 0.2 , which is unexpectedly low for mCVs. A similar picture is seen in spectra of some low-accretion-state polars (e.g. Latham et al. 1981; Kolbin et al. 2024). However, J0720 was in the high state during our observations. There are a few high-state objects with low $EW(\text{He II } 4686)/EW(H\beta)$ ratios. For example, Beuermann et al. (2021) and Oliveira et al. (2020) obtained $EW(\text{He II } 4686)/EW(H\beta) \sim 0.3\text{--}0.4$ for the polar RX J0953.1+1458 with a rather low magnetic field (19 MG). RBS 0490 proposed as a low-field polar shows very strong Balmer lines and has extremely low $EW(\text{He II } 4686)/EW(H\beta) = 0.02\text{--}0.06$ (Joshi et al. 2022). Similar small ratios were derived for the polar candidate CSS1127–05 (Oliveira et al. 2017) and the polar LSQ1725–64 with a low magnetic field (12MG) (Fuchs et al. 2016). In Fig. 13,

the data of $EW(\text{He II } 4686)$ vs. $EW(H\beta)$ for mCVs are presented. Unlike other high-state polars, J0720 does not satisfy Silber’s criterion ($EW(\text{He II } 4686)/EW(H\beta) > 0.4$) at any orbital phase. The reason for this unusually low ratio remains uncertain. The He II 4686 emission can be suppressed by a high magnetic field when cyclotron cooling dominates over bremsstrahlung, and/or via a low accretion rate, which can also lead to a complete absence of He II emission (see, e.g., Kafka et al. 2010).

The X-ray data for J0720 were obtained when it was in the high state. The unabsorbed flux in the 0.2–2.3 keV band obtained from the *eROSITA* data is $F_X^{0.2-2.3 \text{ keV}} \approx 2.3 \times 10^{-13} \text{ erg s}^{-1} \text{ cm}^{-2}$. The flux presented in the XMM-SLEWCLN catalogue is ~ 6 times higher. This is not surprising due to the strong variability of the source. The X-ray spectrum can be well fitted by the thermal plasma model with a temperature compatible with those obtained for other CVs (e.g. Galiullin et al. 2024). Taking these two flux estimates and the optical variability $V \approx 17.3\text{--}20.5 \text{ mag}$, we calculated the X-ray to optical flux ratio $\log(F_X/F_{\text{opt}}) \sim -0.3\text{--}1.8$. Although the X-ray observations do not cover the full orbital period and thus we do not know the exact X-ray flux variation, the derived ratio is in agreement with polars (Schwope et al. 2024; Lin et al. 2025): the majority of polars have $\log(F_X/F_{\text{opt}}) > -1.6$, and a substantial fraction – $\log(F_X/F_{\text{opt}}) > -0.3$.

The accretion rate \dot{M} can be estimated using the bolometric X-ray luminosity $L_{X,\text{bol}}$ via the standard formula

$$L_{X,\text{bol}} \sim GM_1 \dot{M} / R_1, \quad (5)$$

⁶ EWs are presented as positives.

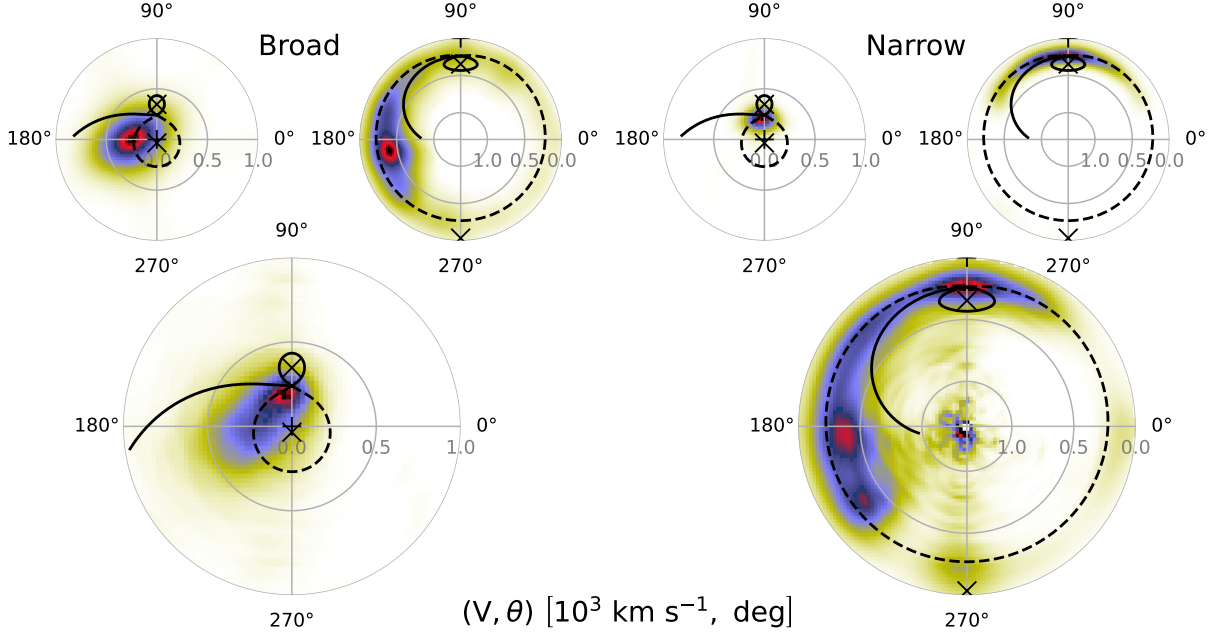


Figure 9. Doppler tomography of the H α line (bottom) and its components (top). The left panels demonstrate the standard Doppler tomograms while the right panels – the inside-out projections. The Roche lobes of the WD and companion (black dashed and solid closed lines, respectively) and the ballistic trajectory (the black curved line) are overlaid. The centre of mass of the system is marked by the cross while that of the WD and companion – by the ‘x’ symbols. The model of the binary system is calculated assuming the white dwarf mass $M_1 = 0.8 M_\odot$, the mass ratio $M_2/M_1 = 0.1$ and the inclination $i = 48^\circ$.

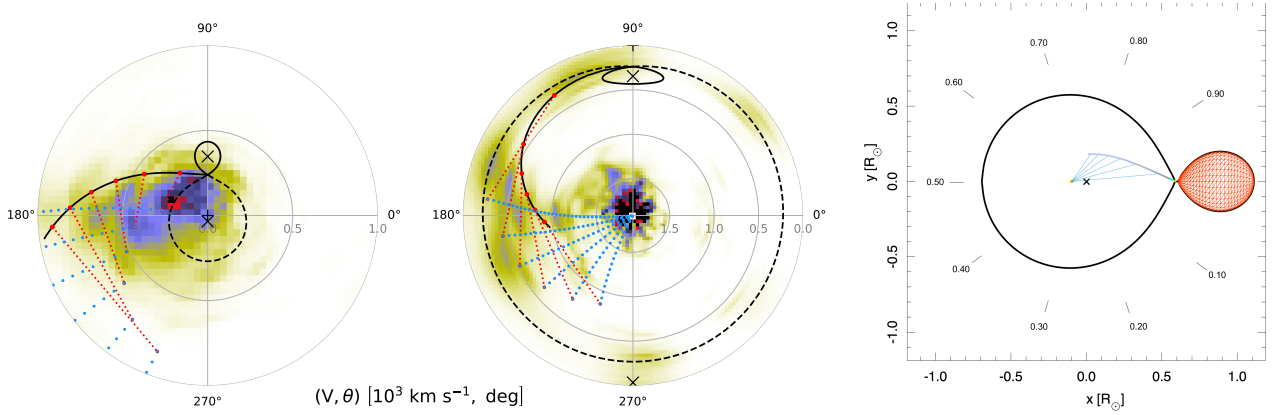


Figure 10. Left and middle panels: Doppler tomography of the He II 4686 line. The left panel demonstrates the standard Doppler tomogram, while the middle panel – the inside-out projection. The designations are the same as in Fig. 9. The dotted lines are magnetic trajectories (see text). Right panel: configuration of the system in spatial coordinates. The magnetic dipole field lines at 10° intervals from 5° to 55° in azimuth around the primary are shown for an example. We assumed the dipole axis azimuth and co-latitude are 27° and 45° . The symbol ‘x’ shows the binary system’s centre of mass. The orbital phases are marked within the plot.

where M_1 and R_1 are the WD mass and radius, and G is the gravitational constant. This transforms into

$$\dot{M} \sim 1.4 \times 10^{-11} D^2 F_{X,\text{bol}} R_1 / M_1 M_\odot \text{ yr}^{-1}, \quad (6)$$

where the distance D is expressed in kpc, the mass M_1 – in Solar masses, the radius R_1 – in 10000 km and the bolometric X-ray flux $F_{X,\text{bol}}$ – in $10^{-12} \text{ erg s}^{-1} \text{ cm}^{-2}$. From the *eROSITA* spectrum, we estimated $F_{X,\text{bol}} \sim 0.7$. The distance can be roughly constrained as follows. As seen from Fig. 1, in the low state of J0720 its minimal optical brightness is $r \sim 21.5$ mag. By analogy with other polars

in the low states, we can assume that the companion dominates in the red part of the optical spectrum. Based on the secondary mass and radius estimated in Sec. 3.3, we assigned it the M5V spectral type as the brightest among other possible later types of stars with similar masses and radii⁷. The absolute magnitude of the M5V type is $M_V = 14.15$. Using the reddening J0720 $E(B-V) = 0.05$ mag and

⁷ https://www.pas.rochester.edu/~emamajek/EEM_dwarf_UBVIJHK_colors_Teff.txt

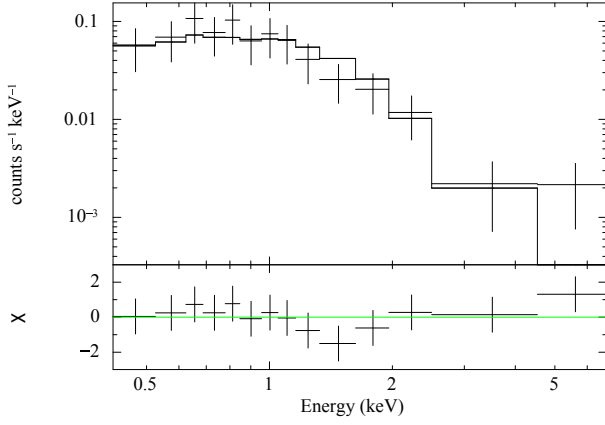


Figure 11. *Top:* the X-ray spectrum of J0720 (crosses) and the best-fitting model TBABS×MEKAL (solid line). For illustrative purposes, the spectrum was grouped to ensure at least 6 counts per bin. *Bottom:* residuals.

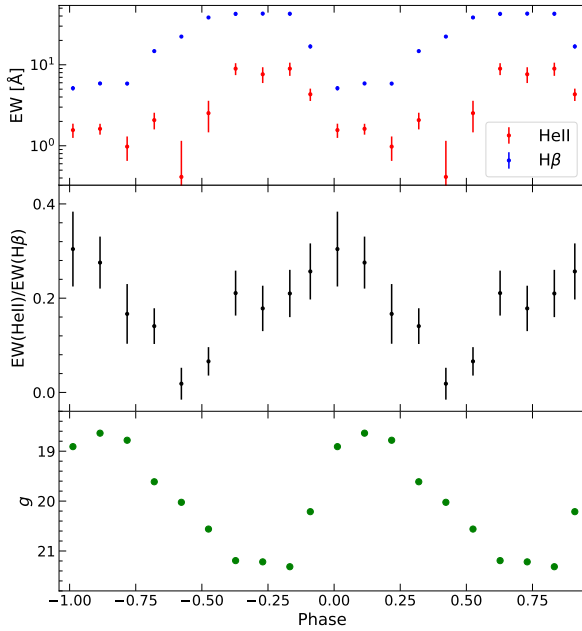


Figure 12. Equivalent widths of the He II 4686 (red dots) and H β (blue dots; top) emission lines, their ratio (middle) and intensity of spectra in the g band (bottom) vs orbital phase.

the transformation equation $r = V - 0.49(B - V) + 0.11$ (Fukugita et al. 1996) with the colour index $B - V = 1.83$, corresponding to the alleged spectral type, we estimated the absolute magnitude $M_r = 13.3$. This results in a distance of ~ 400 pc and $\dot{M} \sim 2 \times 10^{-12} M_{\odot} \text{ yr}^{-1}$. The latter is somewhat lower than that observed for polars in high states (e.g. Beuermann et al. 2021). However, this value should be considered with caution, given the large X-ray flux and distance uncertainties. If the contribution from the secondary to the optical brightness is lower than 21.5 mag, then the distance and \dot{M} would be larger. However, the spectral type can be later, e.g. M6V–M9V, with a larger M_V providing a lower distance.

Although we confirmed that J0720 is a polar, it is not possible to accurately measure the parameters of the binary components and the distance using the current data. The distance will be potentially provided in the future *Gaia* release. Monitoring of J0720 in the optical to reveal it in the low state would be useful to estimate the

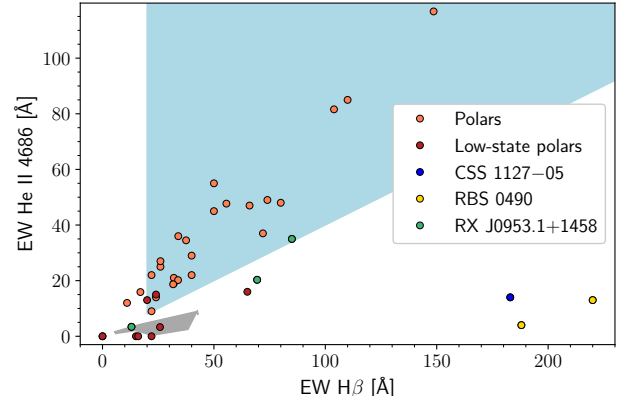


Figure 13. EWs of the He II 4686 vs H β emission lines for different polars in high and low states (orange and dark-red points). The blue area corresponds to the Silver’s criterion for mCVs. The grey region near the low-left corner shows the J0720 position at different orbital phases (see Fig. 12). Measurements for other sources are taken from Oliveira et al. (2017, 2020); Beuermann et al. (2021); Shafer et al. (1995); Joshi et al. (2020, 2022); Voikhanskaya (1986); Singh et al. (1995); Griffiths et al. (1979); Romero-Colmenero et al. (2003); Tovmassian et al. (1997). Sources for which $\text{EW}(\text{He II } 4686)/\text{EW}(\text{H}\beta) < 0.4$ are marked in blue, yellow and green (see text; several points of the same colour correspond to different observations of a specific source).

masses and temperatures of the components. High-resolution optical and infrared spectral observations are needed to search for Zeeman splitting in absorption lines and cyclotron humps in the continuum emission and thus to measure the WD magnetic field. Deeper X-ray observations would provide the orbital flux modulation in this range and help to better constrain the accretion rate. Polarimetric observations are necessary to clarify the system geometry and the magnetic field structure.

ACKNOWLEDGEMENTS

We thank the anonymous referee for useful comments. The work is based on observations made with the GTC telescope, in the Spanish Observatorio del Roque de los Muchachos of the Instituto de Astrofísica de Canarias, under Director’s Discretionary Time and the Observatorio Astronómico Nacional on the Sierra San Pedro Mártir (OAN-SPM), Baja California, México. We thank the daytime and night support staff at the OAN-SPM for facilitating and helping obtain our observations. Based on observations obtained with the Samuel Oschin Telescope 48-inch and the 60-inch Telescope at the Palomar Observatory as part of the Zwicky Transient Facility project. ZTF is supported by the National Science Foundation under Grants No. AST-1440341 and AST-2034437 and a collaboration including current partners Caltech, IPAC, the Oskar Klein Center at Stockholm University, the University of Maryland, University of California, Berkeley, the University of Wisconsin at Milwaukee, University of Warwick, Ruhr University, Cornell University, Northwestern University and Drexel University. Operations are conducted by COO, IPAC, and UW. The CSS survey is funded by the National Aeronautics and Space Administration under Grant No. NNG05GF22G issued through the Science Mission Directorate Near-Earth Objects Observations Program. The CRTS survey is supported by the U.S. National Science Foundation under grants AST-0909182 and AST-1313422. This work used data obtained with eROSITA telescope onboard SRG observatory. The SRG observatory was built by Roskosmos in the interests of the Russian Academy of Sciences represented by its Space

Research Institute (IKI) in the framework of the Russian Federal Space Program, with the participation of the Deutsches Zentrum für Luft- und Raumfahrt (DLR). The SRG/eROSITA X-ray telescope was built by a consortium of German Institutes led by MPE, and supported by DLR. The SRG spacecraft was designed, built, launched and is operated by the Lavochkin Association and its subcontractors. The science data are downlinked via the Deep Space Network Antennae in Bear Lakes, Ussurijsk, and Baykonur, funded by Roskosmos. The eROSITA data used in this work were processed using the eSASS software system developed by the German eROSITA consortium and proprietary data reduction and analysis software developed by the Russian eROSITA Consortium. The work of AVB, AVK, DAZ and YAS was supported by the baseline project FFUG-2024-0002 of the Ioffe Institute (analysis of archival optical data, X-ray data and GTC data obtained on 2024-11-03). SVZ acknowledges the DGAPA-PAPIIT grant IN119323. AYK acknowledges the DGAPA-PAPIIT grant IA105024. The work is partially carried out within the framework of the Project No. BR20280974 "Program of fundamental astrophysical research in Kazakhstan: observations and theory", financed by the Ministry of Education and Science of the Republic of Kazakhstan.

DATA AVAILABILITY

The spectroscopic data are available through the GTC data archive: <https://gtc.sdc.cab.inta-csic.es/gtc/>, CSS data – <http://nesssi.cacr.caltech.edu/DataRelease/>, Pan-STARRS data – <https://catalogs.mast.stsci.edu/panstarrs/>, ZTF data – <https://irsa.ipac.caltech.edu/Missions/ztf.html>, OAN-SPM, MAO, ATO and eROSITA data – upon request.

REFERENCES

- Arnaud K. A., 1996, in Jacoby G. H., Barnes J., eds, *Astronomical Society of the Pacific Conference Series Vol. 101, Astronomical Data Analysis Software and Systems V*. p. 17
- Beuermann K., Burwitz V., Reinsch K., Schwöpe A., Thomas H. C., 2021, *A&A*, **645**, A56
- Bobakov A. V., Kirichenko A. Y., Zharikov S. V., Karpova A. V., Zyuzin D. A., Shibanov Y. A., Mennickent R. E., García-Álvarez D., 2024, *A&A*, **690**, A173
- Brunner H., et al., 2022, *A&A*, **661**, A1
- Cropper M., 1988, *MNRAS*, **231**, 597
- Cropper M., 1990, *Space Sci. Rev.*, **54**, 195
- Davey S., Smith R. C., 1992, *MNRAS*, **257**, 476
- Denisenko D., 2018, *The Astronomer's Telegram*, **11626**, 1
- Drachis P., Romani R. W., Filippenko A. V., Brink T. G., Zheng W., Halpern J. P., Camilo F., 2019, *ApJ*, **883**, 108
- Drake A. J., et al., 2009, *ApJ*, **696**, 870
- Flewellling H. A., et al., 2020, *ApJS*, **251**, 7
- Foight D. R., Güver T., Özel F., Slane P. O., 2016, *ApJ*, **826**, 66
- Foreman-Mackey D., Hogg D. W., Lang D., Goodman J., 2013, *Publications of the Astronomical Society of the Pacific*, **125**, 306–312
- Fuchs J. T., et al., 2016, *MNRAS*, **462**, 2382
- Fukugita M., Ichikawa T., Gunn J. E., Doi M., Shimasaku K., Schneider D. P., 1996, *AJ*, **111**, 1748
- Gaia Collaboration et al., 2016, *A&A*, **595**, A1
- Gaia Collaboration et al., 2023, *A&A*, **674**, A1
- Galiullin I., et al., 2024, *A&A*, **690**, A374
- Green G. M., Schlafly E., Zucker C., Speagle J. S., Finkbeiner D., 2019, *ApJ*, **887**, 93
- Griffiths R. E., Ward M. J., Blades J. C., Wilson A. S., Chaisson L., Johnston M. D., 1979, *ApJ*, **232**, L27
- Joshi A., Pandey J. C., Raj A., Singh K. P., Anupama G. C., Singh H. P., 2020, *MNRAS*, **491**, 201
- Joshi A., Pandey J. C., Rawat N., Raj A., Wang W., Singh H. P., 2022, *AJ*, **163**, 221
- Kafka S., Tappert C., Honeycutt R. K., 2010, *MNRAS*, **403**, 755
- Kolbin A. I., et al., 2024, *Astronomy Letters*, **50**, 335
- Kotze E. J., Potter S. B., McBride V. A., 2016, *A&A*, **595**, A47
- Latham D. W., Liebert J., Steiner J. E., 1981, *ApJ*, **246**, 919
- Liedahl D. A., Osterheld A. L., Goldstein W. H., 1995, *ApJ*, **438**, L115
- Lin J., et al., 2025, *A&A*, **694**, A112
- Liu Y., Hwang H.-C., Zakamska N. L., Thorstensen J. R., 2023, *MNRAS*, **522**, 2719
- Lomb N. R., 1976, *Ap&SS*, **39**, 447
- Marsh T. R., Horne K., 1988, *MNRAS*, **235**, 269
- Masci F. J., et al., 2019, *PASP*, **131**, 018003
- Mata Sánchez D., et al., 2023, *MNRAS*, **520**, 2217
- Mewe R., Gronenschild E. H. B. M., van den Oord G. H. J., 1985, *A&AS*, **62**, 197
- Mewe R., Lemen J. R., van den Oord G. H. J., 1986, *A&AS*, **65**, 511
- Oliveira A. S., Rodrigues C. V., Cieslinski D., Jablonski F. J., Silva K. M. G., Almeida L. A., Rodríguez-Ardila A., Palhares M. S., 2017, *AJ*, **153**, 144
- Oliveira A. S., Rodrigues C. V., Martins M., Palhares M. S., Silva K. M. G., Lima I. J., Jablonski F. J., 2020, *AJ*, **159**, 114
- Pogrosheva T., et al., 2018, *The Astronomer's Telegram*, **11620**, 1
- Predehl P., et al., 2021, *A&A*, **647**, A1
- Prochaska J. X., et al., 2020a, *pypeit/PypeIt: Release 1.0.0*, [doi:10.5281/zenodo.3743493](https://doi.org/10.5281/zenodo.3743493)
- Prochaska J. X., et al., 2020b, *Journal of Open Source Software*, **5**, 2308
- Romero-Colmenero E., Potter S. B., Buckley D. A. H., Barrett P. E., Vrielmann S., 2003, *MNRAS*, **339**, 685
- Salvi N., Ramsay G., Cropper M., Buckley D. A. H., Stobie R. S., 2002, *MNRAS*, **331**, 488
- Saxton R. D., Read A. M., Esquej P., Freyberg M. J., Altieri B., Bermejo D., 2008, *A&A*, **480**, 611
- Scargle J. D., 1982, *ApJ*, **263**, 835
- Schwöpe A. D., Mantel K. H., Horne K., 1997, *A&A*, **319**, 894
- Schwöpe A. D., Horne K., Steeghs D., Still M., 2011, *A&A*, **531**, A34
- Schwöpe A. D., Knauff K., Kurpas J., Salvato M., Stelzer B., Stütz L., Tubin-Arenas D., 2024, *A&A*, **690**, A243
- Shafter A. W., Reinsch K., Beuermann K., Misselt K. A., Buckley D. A. H., Burwitz V., Schwöpe A. D., 1995, *ApJ*, **443**, 319
- Shaw A. W., et al., 2020, *MNRAS*, **498**, 3457
- Silber A. D., 1992, PhD thesis, Massachusetts Institute of Technology
- Singh K. P., et al., 1995, *ApJ*, **453**, L95
- Smith D. A., Dhillon V. S., 1998, *MNRAS*, **301**, 767
- Spruit H. C., 1998, *arXiv e-prints*, pp astro-ph/9806141
- Sunyaev R., et al., 2021, *A&A*, **656**, A132
- Swihart S. J., Strader J., Chomiuk L., Aydi E., Sokolovsky K. V., Ray P. S., Kerr M., 2022, *ApJ*, **941**, 199
- Szkody P., 1998, in Howell S., Kuulkers E., Woodward C., eds, *Astronomical Society of the Pacific Conference Series Vol. 137, Wild Stars in the Old West*. p. 18
- Thomas H. C., Reinsch K., 1996, *A&A*, **315**, L1
- Tovmassian G. H., Greiner J., Zickgraf F. J., Kroll P., Krautter J., Thiering I., Zharykov S. V., Serrano A., 1997, *A&A*, **328**, 571
- Voikhanskaya N. F., 1986, *Soviet Astronomy Letters*, **12**, 196
- Wachter K., Leach R., Kellogg E., 1979, *ApJ*, **230**, 274
- Wilms J., Allen A., McCray R., 2000, *ApJ*, **542**, 914
- Wright E. L., et al., 2019, *AllWISE Source Catalog, NASA IPAC DataSet, IRSA1*, [doi:10.26131/IRSA1](https://doi.org/10.26131/IRSA1)
- Zhao G., Zhao Y.-H., Chu Y.-Q., Jing Y.-P., Deng L.-C., 2012, *Research in Astronomy and Astrophysics*, **12**, 723

This paper has been typeset from a $\mathrm{\TeX}/\mathrm{\LaTeX}$ file prepared by the author.